NUMERICAL INVESTIGATION OF A TWO-DIMENSIONAL BOUSSINESQ SYSTEM

MIN CHEN

Department of Mathematics, Purdue University, West Lafayette, IN 47907, USA

Keywords: water wave, Boussinesq system, Legendre-Galerkin method, rectangular source, super Gaussian, doubly periodic solution, two-dimensional wave pattern

Abstract. We present here a highly efficient and accurate numerical scheme for initial and boundary value problems of a two-dimensional Boussinesq system which describes three-dimensional water waves over a moving and uneven bottom with pressure variation. The scheme is then used to study in details the waves generated from rectangular sources and the two-dimensional wave patterns.

1. Introduction

The understanding of nonlinear wave propagation plays an important role in many branches of science and technology such as oceanography, meteorology, plasma physics and optics. Although considerable progress have been made recently on the theory for full three-dimensional Euler equations [25, 20], the numerical simulations of the three-dimensional water wave equations remain to be a very challenging task, especially when the results are expected in a very short time, such as within an hour or even shorter as in the cases of tsunami so proper warning can be issued. Furthermore, in many practical applications, engineers would prefer a simpler model for water waves, since it has to be associated with other equations, such as a porous media equation for the sediment transportation, or an elastic equations for the sea bottom movement in the cases of tsunamis. Hence, it is important to study in detail some suitable approximations of the three-dimensional water wave equations.

In this paper, the attention is given to a multi-dimensional Boussinesq system which describes approximately the propagation of *small* amplitude and *long* wavelength surface waves in a three-dimensional wave tank filled with an irrotational, incompressible and inviscid liquid under the influence of gravity, moving and/or variable bottom and surface pressure. Denote the moving bottom topography by $\widetilde{h}(x,y,t)$ and the surface pressure variation by $P(x,y,t)$, the system reads (cf. [5, 13, 6] for its derivation and validity),

$$\begin{aligned} &\eta_t + \nabla\cdot\boldsymbol{v} + \nabla\cdot(h+\eta)\boldsymbol{v} - \frac{1}{6}\Delta\eta_t = F(h,P), \\ &\boldsymbol{v}_t + \nabla\eta + \frac{1}{2}\nabla|\boldsymbol{v}|^2 - \frac{1}{6}\Delta\boldsymbol{v}_t = \boldsymbol{G}(h,P), \end{aligned} \tag{1.1}$$

where $h(x,y,t) = \dfrac{\widetilde{h} - h_0}{h_0}$ with h_0 being the average depth of the still water, F and $\boldsymbol{G}$ are the forcing terms involving only derivatives of h and P. In system (1.1), the length scale is taken to be h_0, the average water depth, and the time scale is taken to be $\sqrt{\frac{h_0}{g}}$, with g being the acceleration of gravity.

The dependent variable $\eta(x,y,t)$ represents dimensionless deviation at the spatial point (x,y) at time t of the water surface from its undisturbed position and is a fundamental unknown of the problem. The system (1.1) is a two-space-dimensional equation with $\boldsymbol{v}(x,y,t) \equiv (u,v)$ being the horizontal velocity field at water depth $\sqrt{\frac{2}{3}}h_0$, which is at $z = \sqrt{\frac{2}{3}}$ in the scaled variable. The three-dimensional velocity field $(\boldsymbol{u}(x,y,z,t), w(x,y,z,t))$ at any other location (x,y,z) in the field can be recovered by, due to the small amplitude and long wave assumption,

$$\begin{aligned} \boldsymbol{u}(x,y,z,t) &= \Big(1 + \frac{1}{2}(\frac{2}{3} - z^2)\Delta\Big)\boldsymbol{v}(x,y,t), \\ w(x,y,z,t) &= -z(1 + \frac{1}{3}\Delta)\nabla\cdot\boldsymbol{v}(x,y,t). \end{aligned} \tag{1.2}$$

Some of the special properties of a Boussinesq system, in contrast to the Euler equations, are (a) the system describes a two-space-dimensional (or a three-space-dimensional) wave with an one-space-dimensional (or a two-space-dimensional) system, which reduces the space dimension by one; (b) the dimension of velocity vector consists only horizontal velocity $\boldsymbol{v}$ instead of $(\boldsymbol{u}, w)$; (c) more importantly, the system transforms a free surface problem to a standard problem, namely equations are posed on a fixed domain and are no longer a moving boundary problem. Advantages of (1.1) in comparison with other Boussinesq systems (c.f. [8, 22, 21, 4, 5]) include it contains a smoothing operator $(I - \frac{1}{6}\Delta)^{-1}$ in front of η_t and $\boldsymbol{v}_t$ terms, its phase velocity is bounded and its ease in setting up non-periodic boundary conditions [3]. These features make (1.1) an ideal candidate to use for numerical simulations on many realistic problems.

Mathematical analysis on the system (1.1) has been carried in many aspect. For example, theoretical justification has been provided for the passage from the Euler equations to the Boussinesq systems in the cases that the wave tank has flat bottom and the wave is only acted upon by gravity (see Bona and Colin and Lannes [7]), where the equations read

$$\begin{aligned} A_\eta(\eta, \boldsymbol{v}) &\equiv \eta_t + \nabla\cdot\boldsymbol{v} + \nabla\cdot\eta\boldsymbol{v} - \frac{1}{6}\Delta\eta_t = 0, \\ A_u(\eta, \boldsymbol{v}) &\equiv \boldsymbol{v}_t + \nabla\eta + \frac{1}{2}\nabla|\boldsymbol{v}|^2 - \frac{1}{6}\Delta\boldsymbol{v}_t = 0, \end{aligned} \tag{1.3}$$

and in the cases with variable bottoms (see Chazel [10]). The results state

$$\|(\boldsymbol{u}, w) - \boldsymbol{u}_{euler}\|_{L^\infty(0,t;H^s)} + \|\eta - \eta_{euler}\|_{L^\infty(0,t;H^s)} = O(\epsilon^2 t)$$

for $0 \le t \le O(\epsilon)$, and for s sufficiently large, where ϵ is the ratio of typical wave height over average water depth. (The assumptions on Euler equations used in the proofs are rigorously verified in [2].) The well-posedness and regularity of (1.3) are established in [4, 5]. The existence of line solitary waves, line cnoidal waves, symmetric and asymmetric periodic wave patterns are proved in [12, 11, 14, 15].

System (1.1) can be modified to describe waves with surface tension effects, for example by adding a term $-\tau\nabla\Delta\eta$ or $\tau\Delta\mathbf{v}_t$ on the left-hand side of the second equation, where $\tau = \Gamma/\rho g h_0^2$ is the Bond number, Γ is the surface tension coefficient and ρ is the density of water [16]. Theoretical and numerical investigations for systems with surface tension are similar to that for (1.1) so the discussion in the following sections are carried out for (1.1) for simplicity in notations.

2. Numerical scheme

Denoting the length of the wave tank as H and the width as L (in the scale of h_0), so the physical domain $\Omega = (0, L) \times (0, H)$. At two ends of the tank ($y = 0$ and $y = H$), the solution is required to satisfy prescribed boundary conditions

$$\begin{aligned} \eta(x, 0, t) &= h_0(x, t), \quad \boldsymbol{v}(x, 0, t) = \boldsymbol{v}_0(x, t), \\ \eta(x, H, t) &= h_H(x, t), \quad \boldsymbol{v}(x, H, t) = \boldsymbol{v}_H(x, t). \end{aligned} \tag{2.1}$$

The condition at $y = 0$ models wave motions generated by the wave maker or waves coming from the deep ocean. It is worth to mention that obtaining $(h_0(x,t), \boldsymbol{v}_0(x,t))$ accurately from an experimental set-up is not a trivial issue (e.g. see [19]). On the other end of the tank, $y = H$, the solutions η and $\boldsymbol{v}$ can be set to zero in many cases by taking H large enough, namely by assuming the wave is not yet reaching the other end. (In laboratory experiments, it is more difficult to make the tank as long as desired, so an energy absorbing end might be built to have a similar effect.) Other types of boundary conditions at $y = 0$ and $y = H$, such as a Robin boundary condition can be treated similarly. Across the tank, two types of boundary conditions are considered. One (BC1) is to assume that the solution is periodic across the tank, *i.e.*

$$\text{(BC1)} \qquad \begin{array}{l} \partial_x^m \eta(0,y,t) = \partial_x^m \eta(L,y,t), \\ \partial_x^m \boldsymbol{v}(0,y,t) = \partial_x^m \boldsymbol{v}(L,y,t), \end{array} \quad \text{for} \quad m = 0, 1, 2, \cdots,$$

which has been used in many theoretical and numerical studies for its simplicity. Such treatment will be used in our computations whenever it is justified, simply because a quasi-optimal efficient semi-implicit scheme, which will be described later, can be developed. A physically more relevant set of boundary conditions is (BC2):

$$\text{(BC2)} \qquad \frac{\partial \eta}{\partial x} = 0, \quad u = 0, \quad \frac{\partial v}{\partial x} = 0 \quad \text{at } x = 0 \text{ and } L.$$

It is noted that the boundary conditions at $y = 0$ and $y = H$ should be consistent with (BC1) or (BC2) at four corners of the domain Ω.

The first step of the numerical algorithm is to treat the non-homogeneous boundary conditions at $y = 0$ and $y = H$. Let $Q(x,y,t)$ and $\boldsymbol{V}(x,y,t)$ be the functions satisfy the boundary conditions on all four sides of the domain (linear functions in y are taken in our computations), which is possible because of the consistent constraints. Introducing the new variables

$$\bar{\eta} = \eta - Q(x,y,t), \quad \bar{\boldsymbol{v}} = \boldsymbol{v} - \boldsymbol{V}(x,y,t),$$

the equations under the new variables (for simplicity, the same notations are used) are

$$\text{(2.2)} \qquad \begin{array}{l} A_\eta(\eta, \boldsymbol{v}) + \nabla \cdot (\eta \boldsymbol{V} + Q\boldsymbol{v}) = -A_\eta(Q, \boldsymbol{V}) + F(h,P), \\ A_{\boldsymbol{v}}(\eta, \boldsymbol{v}) + \nabla(\boldsymbol{v} \cdot \boldsymbol{V}) = -A_{\boldsymbol{v}}(Q, \boldsymbol{V}) + G(h,P), \end{array} \quad \text{in } \Omega,$$

with

$$\text{(2.3)} \qquad \eta(x,0,t) = \eta(x,H,t) = 0, \; \boldsymbol{v}(x,0,t) = \boldsymbol{v}(x,H,t) = \mathbf{0},$$

and the homogeneous boundary conditions (BC1) or (BC2) on the boundaries across the tank, namely the $x = 0$ and $x = L$ sides, and a consistent initial condition.

We now describe our numerical scheme for (2.2) and start with the time discretization. Let Δt be the time step size and set $t^n = t^{n-1} + \Delta t$ with $t^0 = 0$. Let η^n and $\boldsymbol{v}^n$ be the numerical approximations of $\eta(x, y, t^n)$ and $\boldsymbol{v}(x, y, t^n)$, with η^0 and $\boldsymbol{v}^0$ being the initial condition. The second-order semi-implicit Crank-Nicolson-leap-frog scheme (with the first step computed by a semi-implicit backward-Euler scheme) will be used. More precisely, let us denote

$$q^0 = \frac{\eta^1 - \eta^0}{\Delta t}, \ \boldsymbol{w}^0 = \frac{\boldsymbol{v}^1 - \boldsymbol{v}^0}{\Delta t} \tag{2.4}$$

and

$$q^n = \frac{\eta^{n+1} - \eta^{n-1}}{2\Delta t}, \ \boldsymbol{w}^n = \frac{\boldsymbol{v}^{n+1} - \boldsymbol{v}^{n-1}}{2\Delta t} \quad \text{for } n \geq 1. \tag{2.5}$$

Then the scheme is to solve h^n and $\boldsymbol{w}^n$ for $n = 0, 1, 2, \cdots$, from

$$\begin{aligned} q^n - \frac{1}{6}\Delta q^n &= (F(h, P) - A_\eta(Q, \boldsymbol{V}) - \nabla \cdot (\eta \boldsymbol{V} + Q\boldsymbol{v}) \\ &\quad - \nabla \cdot \boldsymbol{v} - \nabla \cdot \eta \boldsymbol{v})^n, \\ \boldsymbol{w}^n - \frac{1}{6}\Delta \boldsymbol{w}^n &= (G(h, P) - A_{\boldsymbol{v}}(Q, \boldsymbol{V}) - \nabla(\boldsymbol{v} \cdot \boldsymbol{V}) \\ &\quad - \nabla \eta - \frac{1}{2}\nabla |\boldsymbol{v}|^2)^n, \end{aligned} \tag{2.6}$$

with homogeneous boundary conditions, where the superscripts on the right-hand side mean that the expression is to be evaluated at t^n. After obtaining $(q^n, \boldsymbol{w}^n)$, $(\eta^{n+1}, \boldsymbol{v}^{n+1})$ are direct consequences of (2.4) or (2.5).

Consequently, at each time step, we only have to solve three Poisson type equations of the form

$$u - \frac{1}{6}\Delta u = f \text{ in } \Omega \tag{2.7}$$

with different types of homogeneous boundary conditions as follows.

The boundary conditions for (2.7), in the case of (BC1), are

$$u(x, 0) = u(x, H) = 0, \quad \partial_x^m u(0, y) = \partial_x^m u(L, y), \tag{2.8}$$

with $m = 0, 1, 2. \cdots$, for q^n and the two components $\boldsymbol{w}_1^n$ and $\boldsymbol{w}_2^n$ of $\boldsymbol{w}^n$.

The boundary conditions in the case of (BC2) are

$$u(x, 0) = u(x, H) = 0, \quad u(0, y) = u(L, y) = 0, \tag{2.9}$$

for $\boldsymbol{w}_1^n$ and

$$u(x, 0) = u(x, H) = 0, \quad \partial_x u(0, y) = \partial_x u(L, y) = 0, \tag{2.10}$$

for η and $\boldsymbol{w}_2^n$.

There are existing numerical schemes for solving (2.7) with boundary conditions (2.8), or (2.9) or (2.10). We are going to follow the spectral approximation developed in (cf. [23, 24]) for its efficiency and accuracy. The algorithms will be described in brief for solving a standard problem, namely a equation obtained after rescaling (2.7), so the homogeneous boundary conditions are posed on a standard domain which are independent of H and L.

Consider

$$\widehat{u} - \frac{1}{6}\widehat{\Delta}\widehat{u} = \widehat{f} \text{ in } \widehat{\Omega} \tag{2.11}$$

where $\widehat{\Delta} = a\partial_{rr} + b\partial_{zz}$, with one of the three types of homogeneous boundary conditions (BC):

- case I: Dirichlet zero BC at $z = \pm 1$ and periodic BC across the tank at $r = 0$ and 2π;
- case II: Dirichlet zero BC at $z = \pm 1$ and Dirichlet zero BC across the tank at $r = \pm 1$;
- case III: Dirichlet zero BC at $z = \pm 1$ and Neumann zero BC across the tank at $r = \pm 1$.

One can check easily that a problem (2.7) with (2.8), or (2.9) or (2.10) belongs to one of the cases after a change of variable from y to z and x to r.

Case I: Here, a Fourier-Chebyshev Galerkin method will be used. Namely, let N be an even positive integer,

$$\begin{aligned} V_{NM} = &\text{span}\big\{\phi_l(r)\xi_j(z) : \\ &\qquad l = -\frac{N}{2}, \cdots, -1, 0, 1, \cdots, \frac{N}{2};\ j = 0, 1, \cdots, M-2\big\}, \end{aligned}$$

where $\phi_l(r) = e^{ilr}$, and $\xi_j(z) = T_j(z) - T_{j+2}(z)$ where $T_k(z)$ being the Chebyshev polynomial of degree k. The method is to look for $\widehat{u}_{NM} \in V_{NM}$ such that for $|l| \le \frac{N}{2}$ and $0 \le j \le M-2$,

$$(\widehat{u}_{NM}, \phi_l(r)\xi_j(z)) - \frac{1}{6}(\widehat{\Delta}\widehat{u}_{NM}, \phi_l(r)\xi_j(z)) = (\widehat{f}_{NM}, \phi_l(r)\xi_j(z)), \tag{2.12}$$

where $\widehat{f}_{NM}$ is an interpolation of $\widehat{f}$ at the Fourier-Chebyshev collocation points. Writing $\widehat{u}_{NM} = \sum_{|k|\le\frac{N}{2}} v_k(z)\phi_k(r)$, $\widehat{f}_{NM} = \sum_{|k|\le\frac{N}{2}} f_k(z)\phi_k(r)$ and plugging these into (2.12), we find that (2.12) is reduced to a sequence of one-dimensional problem: find $v_l \in V_M = \text{span}\{\xi_j : j = 0, 1, \cdots, M-2\}$ such that

$$(1 + \frac{1}{6}al^2)(v_l, \xi_j) - \frac{1}{6}b(\partial_{zz}v_l, \xi_j) = (f_l, \xi_j),\ j = 0, 1, \cdots, M-2. \tag{2.13}$$

It is shown in [24] that for each l, (2.13) can be solved in $O(M)$ operations. Since the evaluation of the Fourier-Chebyshev expansion can be done using the Fast Fourier Transform (FFT) in $O(NM\log(NM))$ operations, the total cost of this algorithm for obtaining $\widehat{u}_{NM}$ is $O(NM\log(NM))$ operations, which is quasi-optimal.

Case II and III: Here, we shall adopt a Legendre-Galerkin method. Namely, let

$$\begin{aligned} V_{NM} =& \mathrm{span}\{\phi_l(r)\xi_j(z) : \\ & l = 0, 1, \cdots, N-2;\ j = 0, 1, \cdots, M-2\}, \end{aligned}$$

where $\phi_l(r) = L_l(r) - L_{l+2}(r)$, and $\xi_j(z) = L_j(z) - L_{j+2}(z)$ in case II and $\xi_j(z) = L_j(z) - \frac{j(j+1)}{(j+2)(j+3)}L_{j+2}(z)$ in case III, where $L_k(z)$ being the Legendre polynomial of degree k. We recall that $\phi_l(\pm 1) = 0$, $\xi_j(\pm 1) = 0$ in case II and $\xi_j'(\pm 1) = 0$ in case III (cf. [23]). Hence, the Legendre-Galerkin method is to look for $\widehat{u}_{NM} \in V_{NM}$ such that for $0 \le l \le N-2$ and $0 \le j \le M-2$,

$$(\widehat{u}_{NM}, \phi_l(r)\xi_j(z)) - \frac{1}{6}(\widehat{\Delta}\widehat{u}_{NM}, \phi_l(r)\xi_j(z)) = (\widehat{f}_{NM}, \phi_l(r)\xi_j(z)),$$

where $\widehat{f}_{NM}$ is an interpolation of $\widehat{f}$ at the Legendre-collocation points.

Unlike in the (BC1) case, this problem can not be reduced to a sequence of one-dimension problems since $(\phi_k''(r), \phi_l(r)) \neq c\delta_{kl}$ with c being a constant. However, we shall use the very efficient algorithm developed in [23] whose numerical complexity is roughly $4NM\min(M,N) + O(NM)$.

We recall that in both cases, the algorithms are spectrally accurate. More precisely, we have the following error estimates (cf. [9]):

$$\|\widehat{u} - \widehat{u}_{NM}\|_{H^1(\widehat{\Omega})} \lesssim \min(N,M)^{1-s}\|\widehat{u}\|_{H^s(\widehat{\Omega})} + \min(N,M)^{1-\rho}\|\widehat{f}\|_{H^\rho(\widehat{\Omega})}.$$

In summary, for giving $(\eta^n, \boldsymbol{v}^n)$, $(Q, \boldsymbol{V})^n$ coming from the boundary conditions at $y = 0$ and $y = H$, and $(h, P)^n$ coming from the bottom topography and surface pressure variation, the procedure for obtaining $(\eta^{n+1}, \boldsymbol{v}^{n+1})$ involves

- evaluate the right-hand-side of (2.6) in scaled coordinates (r, z) at points corresponding to the method which is used for solving (2.11). In specific, for case I, they are the Fourier-Chebyshev points, and for case II and III, they are the Legendre-Legendre points;
- solve (2.11) with appropriate boundary conditions;
- obtain $(\eta^{n+1}, \boldsymbol{v}^{n+1})$ with (2.4) or (2.5).

The scheme proposed here is believed to be (i) accurate: spectral accuracy is expected, (ii) efficient: by denoting the number of collocation points as Q, for each time step, $O(Q\log(Q))$ operations are required in the case of (BC1) (quasi-optimal) and $O(Q^{\frac{3}{2}})$ operations are required in the case of (BC2). This is extremely efficient considering the facts that it is a semi-implicit spectral code, and (iii) relatively stable: it is a semi-implicit scheme used on a regularized system.

The numerical testing and simulations performed in Sections 3-5 are for the cases with $P = h = 0$ (system (1.3)) and (BC1), although the scheme is designed for system (1.1) with (BC1) and (BC2). Simulations with nonzero forcing such as a dynamic bottom will appear elsewhere.

3. Numerical testings of the scheme

In this section, an explicit solution

$$
\begin{aligned}
\eta_{exact}(x,t) &= \frac{15}{4}(-2+\cosh(3\sqrt{\frac{2}{5}}\xi))\mathrm{sech}^4(\frac{3\xi}{\sqrt{10}}),\\
u_{exact}(x,t) &= \frac{15}{2}\mathrm{sech}^2(\frac{3}{\sqrt{10}}\xi),
\end{aligned}
\tag{3.1}
$$

with $\xi = x - \frac{5}{2}t - x_0$ of the one-dimensional Boussinesq system (1.3) (the solution is independent of y) is used to check the convergence, accuracy and efficiency of the algorithm. Solution (3.1) is taken because it is the only known non-trivial explicit solution. Although the amplitude of this solutions is big and it travels fast, which is outside the range of validity of system (1.1), it should be a good testing case for the accuracy (worst case scenario) of the numerical code. It may not be a good testing case for the stability of the scheme since we do not know the stability of this particular solution.

We will only present the result for the scheme with (BC1), since it will be used in the next section.

3.1. Efficiency and accuracy of x-discretization.

We let the exact y-independent line traveling wave solution (3.1) propagate in the x-direction from time 0 to T and compare the resulting numerical solution with the exact solution $(\eta_{exact}(x,T), u_{exact}(x,T), 0)$.

In specific, the computation is carried out in the domain $[0,22]\times[0,20]$ and for $T = 1$ where the wave has traveled about half of the wave length. The reason for choosing $T = 1$, which is not as big as one may expect, will be explained in Section 3.2.

The initial data is taken to be

$$(\eta(x,y,0), u(x,y,0), v(x,y,0)) = (\eta_{exact}(x,0), u_{exact}(x,0), 0)$$

n	CPU(s)	E_η^∞	E_u^∞	E_v^∞
32	0.16(s)	0.70	0.26	0.12
64	0.38(s)	1.8E-3	1.5E-3	3.0E-4
96	0.42(s)	2.4E-6	1.5E-6	5.8E-7
128	0.80(s)	1.73E-6	9.7E-7	5.8E-7
192	1.08(s)	1.77E-6	9.8E-7	5.8E-7

Table 1. CPU time used in one time step and errors in the numerical solution at $T = 1$ when $\Omega = (0, 22) \times (0, 20)$, $\Delta t = 0.0001$ and using $(n, 512)$ modes in x and y directions respectively.

with $x_0 = 10$. The boundary condition on the ends of the wave tank are

$$(\eta(x, 0, t), u(x, 0, t), v(x, 0, t)) = (\eta_{exact}(x, t), u_{exact}(x, t), 0),$$
$$(\eta(x, H, t), u(x, H, t), v(x, H, t)) = (\eta_{exact}(x, t), u_{exact}(x, t), 0),$$

while the periodic boundary conditions are used at $x = 0$ and $x = 22$. Clearly, the problem to be solved is (1.3) with (BC1).

We isolate the x-discretization error by taking small time stepsize $\Delta t = 0.0001$ and large number of modes in y-direction ($m = 512$), so the error from x-discretization is dominating. The number of modes in x-direction, n, is taken to be $32, 64, 96, 128, 196$ and we record in Table 1 the CPU time used for one time step (the last one) and the max-norms of the errors in η, u and v (E_η^∞, E_u^∞ and E_v^∞), for each n, where

$$E^\infty_{(\eta,u,v)} = \max_{1\le i\le n, 0\le j\le m} |(\eta, u, v)^N(x_i, y_j, T) - (\eta, u, 0)_{exact}(x_i, T)|$$

with (x_i, y_j) being the Fourier-Legendre points and $N\Delta t = T$.

The structure of Table 1 is as follows. The first column corresponds to the number of modes in x direction and the second column presents the CPU time used to obtain the numerical solution for one time step. The third, fourth and fifth columns show the maximum absolute errors at collocation points between the exact solution and corresponding numerical approximation. We first note that the errors in all three components decrease dramatically when n changes from 32 to 64 and from 64 to 96. With 96 modes in x-direction, the numerical solution is very accurate already. We also note that the accuracy of the numerical solutions do not improve when n increases from 128 to 192, which indicates that at $n = 128$ and 192, the time-discretization error becomes dominate.

m	CPU(s)	E_η^∞	E_u^∞	E_v^∞
64	0.06(s)	0.12	0	0.14
96	0.17(s)	2.6E-3	0	2.0E-3
128	0.26(s)	3.2E-5	0	1.5E-5
192	0.46(s)	1.7E-6	0	9.5E-7
256	0.6(s)	1.7E-6	0	9.5E-7

TABLE 2. CPU time used in one time step and errors in the numerical solution at $T = 1$ when $\Omega = (0, 20) \times (0, 22)$, $\Delta t = 0.0001$ and using $(512, m)$ modes in x and y directions respectively.

3.2. **Efficiency and accuracy of y-discretization.** In a similar way, we analyze the efficiency and accuracy of y-discretization by letting the line traveling wave, independent of x, propagate in y direction. The Legendre, instead of Fourier, approximation is therefore tested. The initial data is taken to be

$$(\eta(x, y, 0), u(x, y, 0), v(x, y, 0)) = (\eta_{exact}(y, 0), 0, u_{exact}(y, 0)) \tag{3.2}$$

with boundary data at $y = 0$ and $y = H$ being zero and the boundary condition at $x = 0$ and $x = L$ being periodic. This is again an equation (1.3) with (BC1), and with homogeneous boundary conditions at $y = 0$ and $y = H$.

The CPU time used in one time step (the last one) and errors in the numerical solution at $T = 1$ when $\Omega = (0, 20)\times(0, 22)$, $\Delta t = 0.0001$ and using $(512, m)$ modes in x and y directions respectively are recorded in Table 2. We again note that the error decreases dramatically when m changes from 64 to 96 and from 96 to 128. It appears that 128 modes in y-direction is suffice for most of the calculations. Table 2 also indicates that at $m = 192$ and 256, the time-discretization error becomes dominate.

We also carried out the computation for $T = 10$ on $\Omega = (0, 10) \times (0, 45)$ with various number of modes in x- and y-directions. The result for $n = 64$, $m = 128$ and $\Delta t = 0.001$ is shown in Figure 1 along with the exact solution. We first notice that from Figure 1(a) that even with relatively small number of modes, 128 for an interval of length 45, the agreement between the exact solution and the corresponding numerical approximation is very good (the two lines are almost not distinguishable). One therefore expect that the errors E_η^∞, E_v^∞ and E_u^∞ to be very small. But this is not the case. In fact, $E_\eta^\infty = 0.619$, $E_v^\infty = 0.421$ and $E_u^\infty = 0$. By zooming in the area of y from 33 to 37,

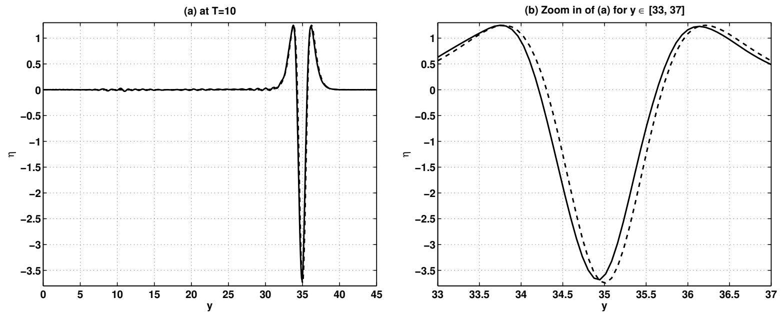

FIGURE 1. (a) Comparison of numerical solution, plotted using spline, (solid line) and the exact explicit solution (dashed line) at $T = 10$; (b) zoom in of (a) for $y \in [33, 37]$.

it is noted that the error is mainly due to a phase speed difference. It is for the purpose of limiting the effect of error caused by the phase speed difference, we took $T = 1$ for the computations carried out for Table 1 and 2 (cf. [1] for more on error from a phase shift).

A comparison between the spectral method and the method proposed in [3] which is based on a numerical integration can be made here. Using $\Delta t = 0.001$ and $H = 40$ as in [3], the error E_η^∞ is about 1.68E-4 with $m = 256$ modes in y direction. In comparison, according to Table 1 in [3], $\frac{40}{0.25^3} = 2560$ mesh points will provide the approximate solution with error 4.5E-4, about 2.5 times of more error with about 10 times more mesh points (modes). Therefore, it is concluded, as expected, that the spectral method is much more efficient. However, there is a big advantage associated with the method proposed in [3], it is unconditional stable!

4. Simulation on Waves generated by a rectangular source

In many real physical situations, the wave is generated by a source which is not necessarily axisymmetric. For example, in the 2004 Asian Tsunami, the waves were generated by a fault line which is about 1200km long in a nearly north-south orientation. It is observed that the greatest strength of the tsunami waves was in an east-west direction [18].

This sequence of numerical simulations is designed to study the waves generated from rectangular sources. We first study the phenomena with an initially raised water level in a nearly rectangular area with aspect ratio 10. We then compare the waves generated from sources with different aspect ratios. Finally, the effects of the initial amplitude, the structure of initial water surface on the resulting waves are investigated.

Let the domain of the integration be $[0, 240] \times [0, 240]$, x_0 and y_0 be 120, and the initial data in this sequence of tests be based on

$$\begin{aligned} &\eta(x,y,0) = \eta_\sigma(x,y) \equiv 5\alpha^2 e^{-\alpha^{2m}(\sigma^m (x-x_0)^{2m} + \sigma^{-m}(y-y_0)^{2m})}, \\ &u(x,y,0) = 0, \end{aligned} \tag{4.1}$$

where $\alpha = 0.1$, $m = 8$. By taking $m = 8$, the initial wave profile is similar to having water level raised in a localized area which is approximately $20/\sqrt{\sigma}$ times $20\sqrt{\sigma}$ (aspect ratio σ) in the middle of the wave tank. The super Gaussian, instead of a two-dimensional boxcar function, is used because its smoothness. It is worth to note that with these initial data, the amplitude, $\max(\eta_\sigma(x,y))$, at $t = 0$ is 0.05 and the volume $\int\int \eta_\sigma(x,y)dxdy$ is $5\Big(\int e^{-x^{2m}}dx\Big)^2$ which are both independent of the aspect ratio σ. In the simulations carried out in Section 4, 1024 modes are taken in x and y directions and the time step size is taken to be 0.025. It is worth to mention that in all figures, the scales used in the horizontal directions could be very different from the scale in the vertical direction.

4.1. **Start from raised water level and $\sigma = 10$.** We first examine the resulting waves started from a north-south oriented raised water level. The initial data is (4.1) with $\sigma = 10$. The total CPU time used for this computation, with 1024×1024 modes and 3600 time steps ($T = 90, \Delta t = 0,025$), is 21.8 hours with the use of a Dell precision workstation 530 (2.0GHz).

In Figure 2, the initial wave profile $\eta(x,y,0)$ and its contour plot are presented to give a view on the rectangular nature of the initial data. Similar plots are presented in Figure 3 for $t = 60$. We observe from Figure 3 that the leading wave in the positive and negative x-directions (east-west directions) are much bigger than that in the north-south directions. In addition, there is a big trough, which might be partially responsible to a water withdraw near beaches for the ocean waves, following the leading wave in the east-west directions. The waves in the north-south directions are very small. These observations are confirmed by graphs in Figure 4, which shows the surface profile with respect to x at $y = 120$ and that with respect to y at $x = 120$, both at $t = 60$.

We now analyze the locations and the heights of the leading waves. The wave front can be observed easily from the contour plots, namely from Figures 2(b) and 3(b). At $t = 60$, it is in an ellipse shape. It is expected that as t increases, the wave front will be getting more close

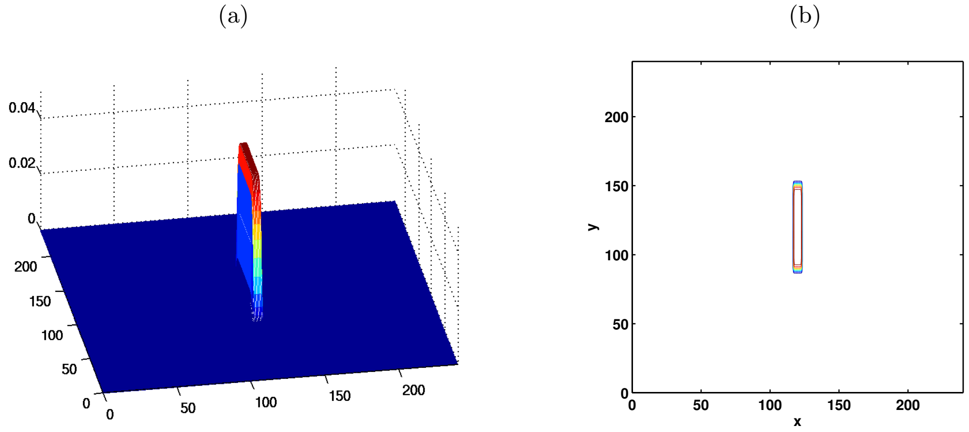

FIGURE 2. Start from raised water level with $\sigma = 10$: plots of initial condition $\eta(x, y, 0)$ with (a) surface profile; (b) contour plot.

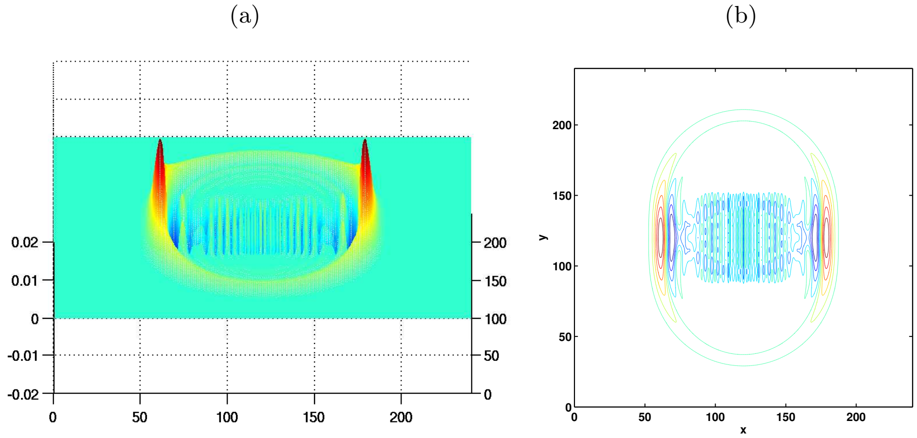

FIGURE 3. Start from raised water level with $\sigma = 10$: plots of $\eta(x, y, 60)$ with (a) surface profile; (b) contour plot.

to a circle by the fact that larger wave travels faster. Quantitatively, let $x^*(t)$ be the distance between the location of the x-directional leading wave at $y = y_0$ and the center (x_0, y_0) at time t, so $\eta(120 - x^*(t), 120, t)$ is the first local maximum of the function $\eta(x, 120, t)$ for x in $[0, 240]$. Similarly, let $y^*(t)$ be the the distance between the location of y-directional leading wave at $x = x_0$ and the center (x_0, y_0). Figure 5(a) shows $x^*(t)$ (solid line) and $y^*(t)$ (dashed line) and figure 5(b) shows the heights of the leading waves, namely $hx(t) \equiv \eta(120 - x^*(t), 120, t)$ (solid line) and $hy(t) \equiv \eta(120, 120 - y^*(t), t)$ (dashed line). Another

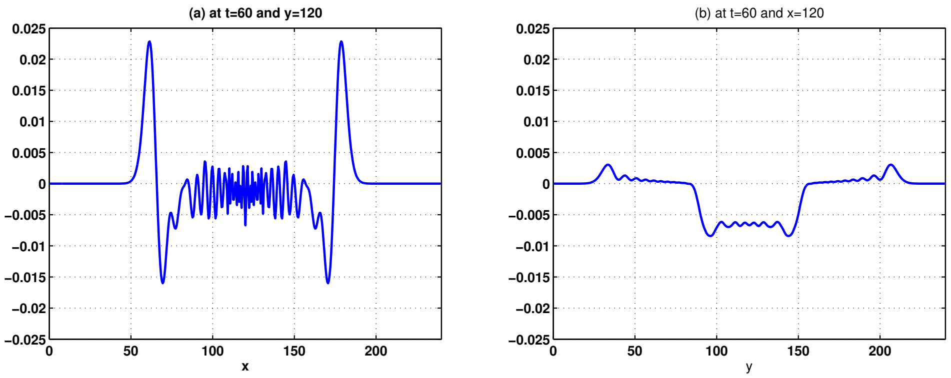

FIGURE 4. Start from raised water level with $\sigma = 10$: plots of (a) $\eta(x, 120, 60)$ and (b) $\eta(120, y, 60)$.

way to compare the leading waves in x- and y-directions is by comparing them with respect to their distances to the epicenter. Figure 6 is for that purpose which shows $hx(x^*)$ and $hy(y^*)$ and the ratio between $hx(x^*)$ and $hy(y^*)$.

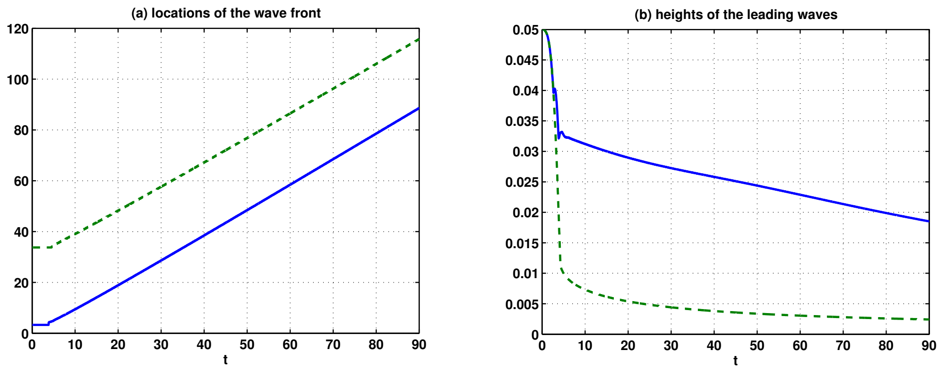

FIGURE 5. Start from raised water level with $\sigma = 10$: (a) distances between the epicenter (x_0, y_0) and the wave fronts of x- and y-directional waves, $x^*(t)$ (solid line) and $y^*(t)$ (dashed line); (b) heights of the x- and y-directional leading waves, $hx(t)$ (solid line) and $hy(t)$ (dashed line).

The observations from Figures 2-6 are

- the height of the x-directional leading wave is much bigger than that of the y-directional leading wave at any time t. As time evolves, the ratio ($hx(t)/hy(t)$) is between 7 and 8 for t between 45 and 90 (c.f. Figures 3(a), 4, 5(b));

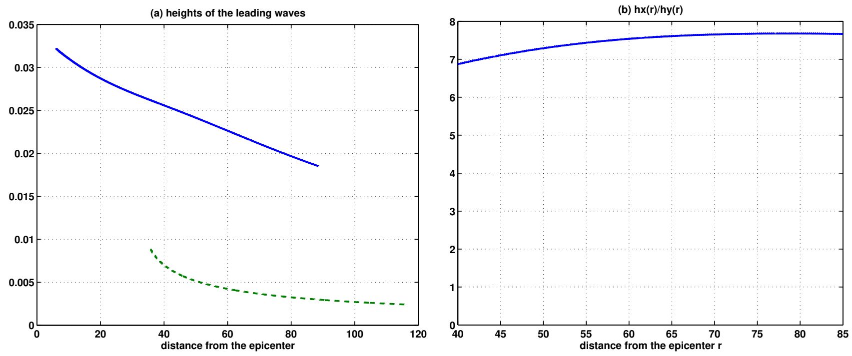

FIGURE 6. Start from raised water level: (a) $hx(r)$ (solid line) and $hy(r)$ (dashed line); (b) $hx(r)/hy(r)$, with $r = x^* = y^*$.

- the location of the leading wave form an "ellipse" shape (c.f. Figure 3(b)). The leading waves in x- and y- directions move with about constant speeds. With a least-square linear fitting on the data from $t = 45$ to $t = 90$ which is chosen to avoid the immediate transition area, one finds that the semi-major axes $y^*(t)$ is approximately $0.97t + 28$ (the approximation of the dashed line in Figure 5(a)) and semi-minor axes $x^*(t)$ is approximately $1.0t - 1.8$ (the approximation of the solid line in Figure 5(a)). The speed of the propagation of semi-minor is larger than that of semi-major, so the location of the wave fronts will form a more round shape as time evolves;
- after the leading waves have formed, namely when r-the distance from the epicenter, larger than 40, the ratio between the heights of the x- and y-directional leading waves is increasing with respect to r and between 6 and 8 for r between 40 and 85.

4.2. **Start from raised water level with $\sigma = 1, 2, 4, 6, 8, 10$.** The goal of this sequence of tests is to observe and analyze the effect of σ. Specifically, two-dimensional super Gaussian functions (4.1) with $\sigma = 1, 2, 4, 6, 8, 10$, which have fixed amplitude and volume but various aspect ratio, were used as initial water deviations. It is observed, as reported in the cases of tsunamis, that when the longer sides of the rectangle are on the north-south orientation, the waves in the east-west directions are bigger. In fact, the bigger the aspect ratio between the longer sides and the shorter sides, the bigger the waves in the east-west directions and the smaller the waves in the north-south directions.

	$\sigma = 1$	$\sigma = 2$	$\sigma = 4$	$\sigma = 6$	$\sigma = 8$	$\sigma = 10$
$x^*(90)$	95	92	90	90	89	89
$hx(90)$	8.8(−3)	1.2(−2)	1.6(−2)	1.8(−2)	1.8(−2)	1.9(−2)
$y^*(90)$	95	99	104	109	112	116
$hy(90)$	8.8(−3)	6.1(−3)	4.2(−3)	3.3(−3)	2.8(−3)	2.4(−3)
$hx/hy(90)$	1.0	2.0	3.9	5.4	6.6	7.6

TABLE 3. Start from raised water level and compare the locations, the heights and the ratio between the heights of x- and y-directional leading waves at $T = 90$ when aspect ratio $\sigma = 1, 2, 4, 6, 8, 10$.

In Table 3, the locations of the x-leading wave at $y = y_0 = 120$ and the y-leading wave at $x = x_0 = 120$ at $t = 90$, $x^*(90)$ and $y^*(90)$, the corresponding heights, $hx(90)$ and $hy(90)$ and the ratio $hx(90)/hy(90)$ are reported for each σ. It is observed that,

- as σ increases, the heights of x-directional leading waves increase. As σ increases from 1 to 10, the wave heights more than doubled (see row 3 of Table 3);
- as σ increases, the x-directional leading waves are closer to the epicenter (x_0, y_0) (see row 2 of Table 3). This appears at odd at first sight until one realizes that it started at a different place, namely about 10 for $\sigma = 1$ and about 3 for $\sigma = 10$ (approximately $10/\sqrt{\sigma}$ for any σ);
- as σ increases, the heights of y-directional leading waves decrease. As σ increases from 1 to 10, the heights decrease from 0.0088 to about 27% of 0.0088 (see row 5 of Table 3);
- the combination of increasing heights in x-directional waves and decreasing heights in y-directional waves, as σ increases, yields the heights' ratio between x-directional and y-directional waves increases. At $\sigma = 10$, the ratio is about 7.6 (see row 6 of Table 3).

It is worth to note again that these experiments are conducted with initial wave profiles having identical volume and height, vary only with aspect ratio σ. It is then concluded that a key factor in deciding the heights of the leading waves generated from a rectangular source is the aspect ratio.

4.3. **Start from raised water level with $\sigma = 10$, but 10 times higher than that in Section 4.1.** To test the effect of nonlinearity, an experiment with bigger initial data, $\eta(x, y, 0) = 10\eta_{10}(x, y)$ is conducted. The contour plot of wave surface, $\eta(x, y, 60)$, and the wave profile with respect to x at $y = 120$, $\eta(x, 120, 60)$, at $t = 60$ are shown in Figure 7. The qualitative properties are the same as the case in Section 4.1. But quantitatively, by comparing Figure 7(b) with Figure 4(a), one sees that the x-directional leading wave is more than 10 times bigger than the case with initial data $\eta_{10}(x, y)$, which is a nonlinear effect. Furthermore, the x-directional leading wave moves slightly faster than that in Section 4.1, approximately with $x^*(t) = 1.13t+0.99$. The location of the y-directional leading wave satisfies approximately $y^*(t) = 0.99t + 29$.

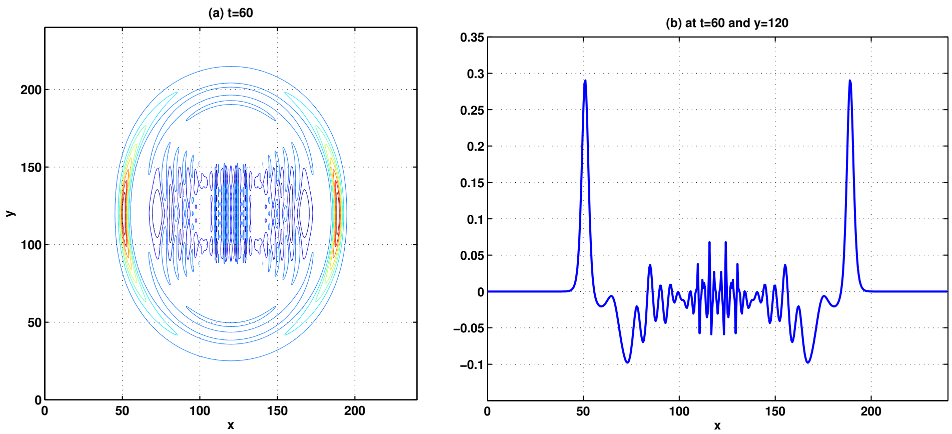

FIGURE 7. Start from higher initial water displacement: plots of (a) $\eta(x, y, 60)$; (b) $\eta(x, 120, 60)$.

4.4. **Start from lowered water level with $\sigma = 10$.** To observe the effect of different types of initial water surface, this numerical simulation starts with $\eta(x, y, 0) = -\eta_{10}(x, y)$, lowered water level in an approximately rectangular region. The wave surface, $\eta(x, y, 60)$, is shown in Figure 8(a) and the wave profile with respect to x at $y = 120$ is shown in Figure 8(b). It is observed that the x-directional waves start with a trough, which might be a contributing factor for the initial water withdraw during a tsunami, and followed by a leading positive wave. The second wave is almost well-developed at $t = 60$ which is very different from the case in Section 4.1. By comparing 8(b) with Figure 4(a) in Section 4.1, it is noticed that the leading positive wave is about

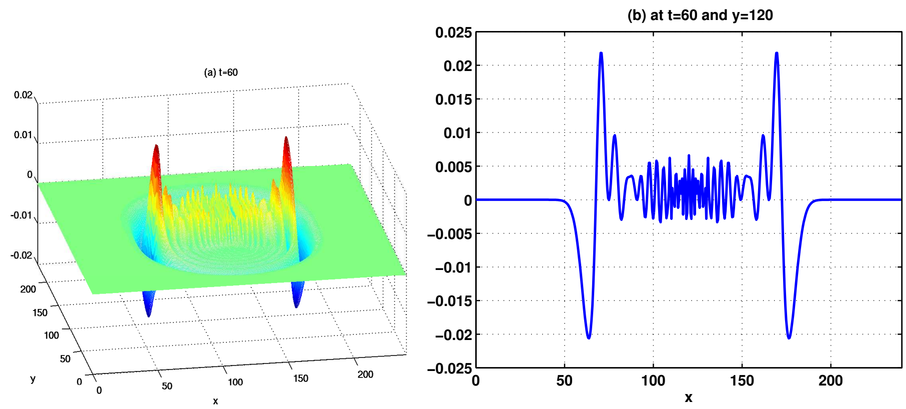

FIGURE 8. Start from lowered water level with $\sigma = 10$: plots of (a) $\eta(x, y, 60)$; (b) $\eta(x, 120, 60)$.

the same size. Again, the y-directional leading wave is very small when compared with the x-directional leading waves.

4.5. **Start from raised and lowered water level with $\sigma = 10$.** The last experiment in this sequence is with the combination of raised and lowered initial water level. It is designed to understand the effect of different types of eruptions along the fault line, as it occurs in nature such as in the 2004 Tsunami. The initial wave profile is given by

$$\eta(x, y, 0) = \eta_{10}(x, y) \tanh(10(y - y_0)) \tag{4.2}$$

which is, in an area of approximately 6.32×62.4, the northern half ($y > 120$) has a raised water level and the southern half ($y < 120$) has a lowered water level. The hyperbolic tangent function is used for its smoothness.

The water profiles at $t = 60$ and $t = 90$ are plotted in Figure 9, one in the format of surface profile and one in the format of contour plot. The resulting wave in the northern half starts with an elevation and then a trough, and in the southern half, a trough and then an elevation. The y-directional waves are significantly smaller than the x-directional waves as in all the cases with large aspect ratios. The x-directional waves at $y = 95.88, 105.3, 134.0, 149.1$ are plotted in Figure 10 to show in details the different structures of the waves when varying y. The second wave could be bigger than the first wave depend on the time and the y-location. An example of such case is at $y = 134.0$ where the x-directional wave starts with an elevation, then a big trough and then followed by a bigger wave. Such phenomena were observed during tsunamis.

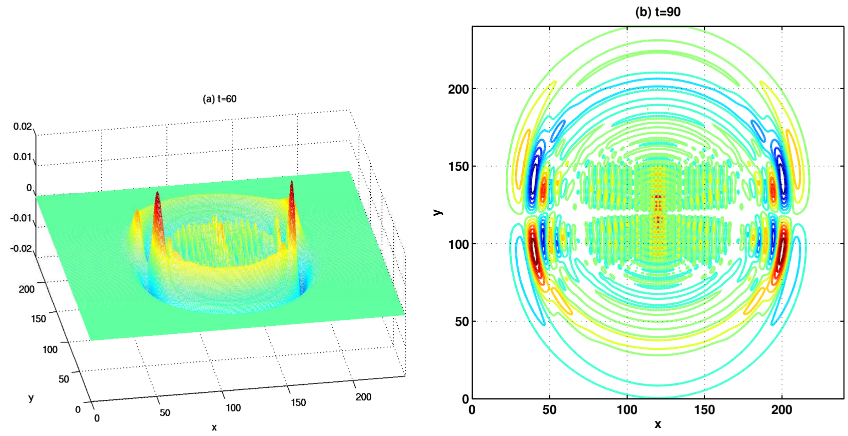

FIGURE 9. Start from raised and lowered initial surface: plots of (a) $\eta(x, y, 60)$; (b) $\eta(x, y, 90)$.

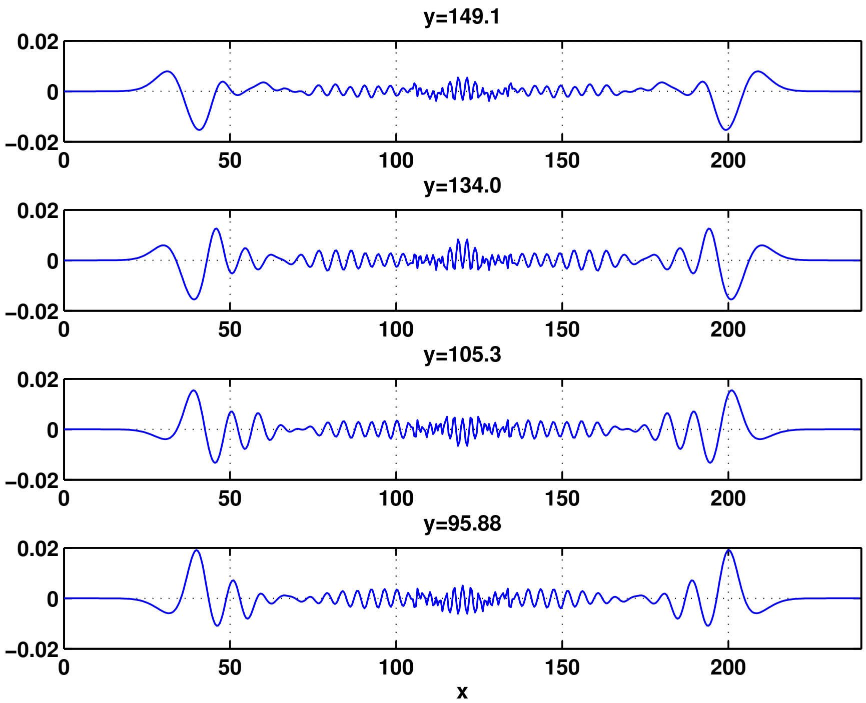

FIGURE 10. Start from raised and lowered initial surface: plots of wave profile at $y = 95.88, 105.3, 134.0, 149.1$ and at $t = 90$.

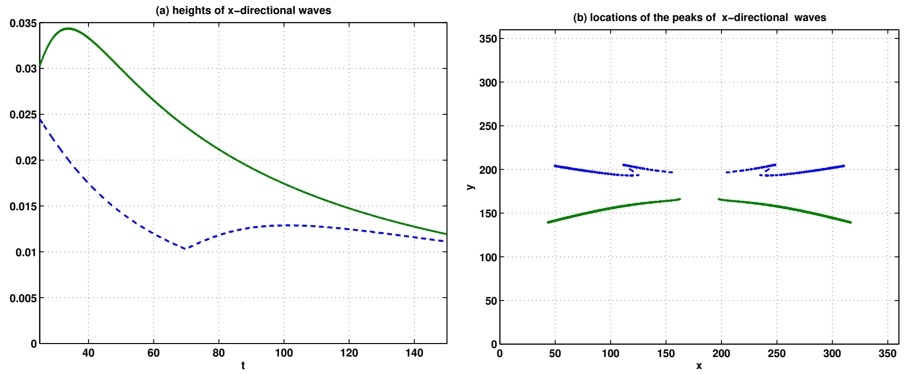

FIGURE 11. Start from raised and lowered initial surface: plots of (a) heights of x-directional waves and (b) locations of the peaks of the x-directional waves.

In Figure 11(a), the heights of the x-directional positive waves in the northern half (dashed line) and in the southern half (solid line) are plotted for time t after the initial transition period. The southern half has larger waves, although it started with a trough. In northern part, the first wave is bigger until t is about 69. From that point, the second wave is bigger. By comparing Figure 11(a) with Figure 5(b), it is observed that for $t < 80$, the maximum amplitude of x-directional wave (which happens in the lower half) is bigger than that in the case with only raised water level. The locations where the maximum wave heights occur in the northern and southern halves are plotted in Figure 11(b).

5. Two-dimensional periodic wave patterns

In this section, two dimensional wave patterns are generated by boundary conditions. It is designed to simulate the waves generated by wave makers, exactly as in the laboratory experiments or in the fields [19]. It is worth mentioning that no filters are used in our computation, as compared to previous numerical simulations such as in [17], and zero initial data, instead of an initial data which is close to the steady solution of a traveling wave, is used.

There are three parameters, which are adjustable and called control parameters in experiments, related to the input boundary conditions at the wave maker end $y = 0$. We denote them by k_x the x-directional wave number, k_t the t-directional wave number which corresponding to the frequency of the wave maker and ϵ the amplitude of the wave at the wave maker which corresponding to the wave peddles' amplitude.

The boundary condition is given by

$$\begin{pmatrix} \eta(x,0,t) \\ u(x,0,t) \\ v(x,0,t) \end{pmatrix} = \begin{pmatrix} \epsilon \sin(k_t t)\cos(k_x x) \\ -\frac{\epsilon k_x}{\sqrt{k_x^2+k_y^2}} \cos(k_t t)\sin(k_x x) \\ \frac{\epsilon k_y}{\sqrt{k_x^2+k_y^2}} \sin(k_t t)\cos(k_x x) \end{pmatrix} \tag{5.1}$$

where (k_x, k_y, k_t) satisfies the linear dispersion relation, namely

$$(1 + \frac{1}{6}(k_x^2 + k_y^2))^2 k_t^2 - (k_x^2 + k_y^2) = 0. \tag{5.2}$$

For any fixed k_x and k_t, k_y which is positive is determined by (5.2). When more than one choices are given, the smaller one will be used so the solution is in the long wave range.

In this set of simulations, the computation domain is taken to be $(0, \frac{2\pi}{k_x}) \times (0, 200)$. The boundary condition at $y = 200$ is taken to be zero and the boundary conditions across the wave tank is taken to be periodic. Several separate computations were conducted with (BC2) and the results showed no difference with the computations performed with (BC1). The solutions obtained with (BC1) actually satisfy the boundary condition (BC2) (see also Figure 14).

With this set of initial and boundary conditions, the consistency conditions between the four sides of the boundaries are satisfied. But the consistency condition between the initial condition and the boundary conditions at $y = 0$ is violated in the u component. Since it did not generate any trouble during the computations, we did not smooth it out artificially.

The computation is conducted with 256 modes in x-direction, 1024 modes in y-direction, and time stepsize 0.04. When the functions or surfaces are plotted against x, two or more x-periods are graphed for clarity.

5.1. **Comparison with an explicit approximate solution of small amplitude.** Using a perturbation approach, it is shown in [14] that (1.3) admits two-dimensional doubly periodic solutions. The corresponding traveling solution of *linearized equations* with this set of boundary condition (when ϵ small) reads

$$\begin{pmatrix} \eta(x,y,t) \\ u(x,y,t) \\ v(x,y,t) \end{pmatrix} = \begin{pmatrix} -\epsilon \sin(k_y y - k_t t)\cos(k_x x) \\ -\frac{\epsilon k_x}{\sqrt{k_x^2+k_y^2}} \cos(k_y y - k_t t)\sin(k_x x) \\ -\frac{\epsilon k_y}{\sqrt{k_x^2+k_y^2}} \sin(k_y y - k_t t)\cos(k_x x) \end{pmatrix} \tag{5.3}$$

which is the leading term of the full perturbation solution.

We now compare the numerical solution of the partial differential equations with (5.3). The boundary data in the numerical simulation is taken to be (5.1) with $\epsilon = 0.05$, $k_t = 0.5$ and $k_x = 0.13$, which yields $k_y = 0.5064$, and the computation domain is $[0, 48.33] \times [0, 200]$. The solution at $t = 170$ is plotted in Figure 12(a). The pattern is moving in the y direction, downward. The crest is lighter and the trough is darker. It is clear that a steady traveling two-dimensional doubly periodic pattern is formed. Figure 12(a) demonstrates numerically the existence and stability of two-dimensional doubly periodic waves of small amplitude. Figure (12)(b) shows the corresponding leading term of the perturbation solution (5.3) with $t = 170$. By comparing the two patterns, one sees that the wave numbers in x- and y- directions and the traveling speed of the patterns are about the same, which confirms the theoretical analysis in [14] and also validates again the numerical algorithm.

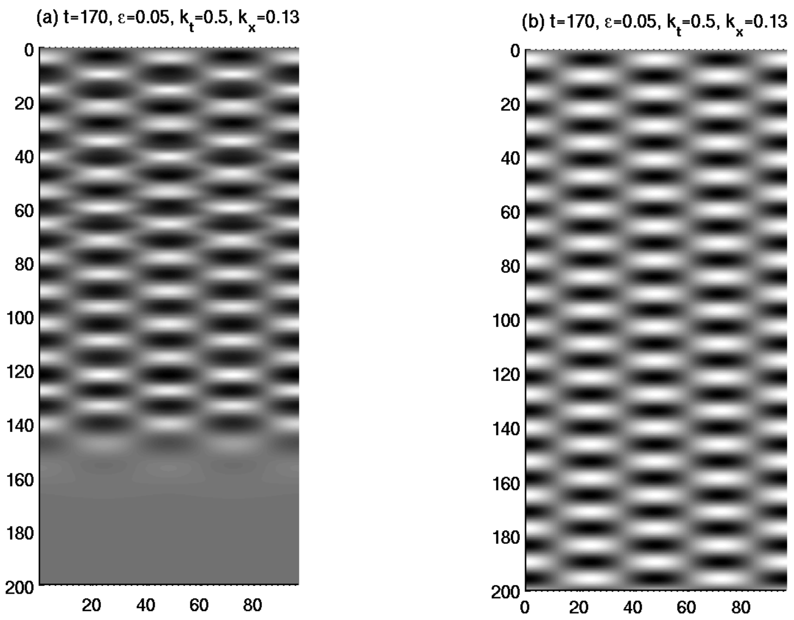

FIGURE 12. (a) Numerical solution of (1.3) with boundary condition (5.1) where $\epsilon = 0.05$, $k_x = 0.13$, $k_t = 0.50$, $k_y = 0.5064$ and $t = 170$; (b) (5.3) with the same parameters.

5.2. **Wave patterns with various ϵ.** The goal of this subsection is to investigate the changes of wave patterns when the wave paddles' amplitude changes. The same set of parameters as in Section 5.1 are used, except in addition to $\epsilon = 0.05$, we will also study the cases with $\epsilon = 0.16, 0.3$ and 0.5.

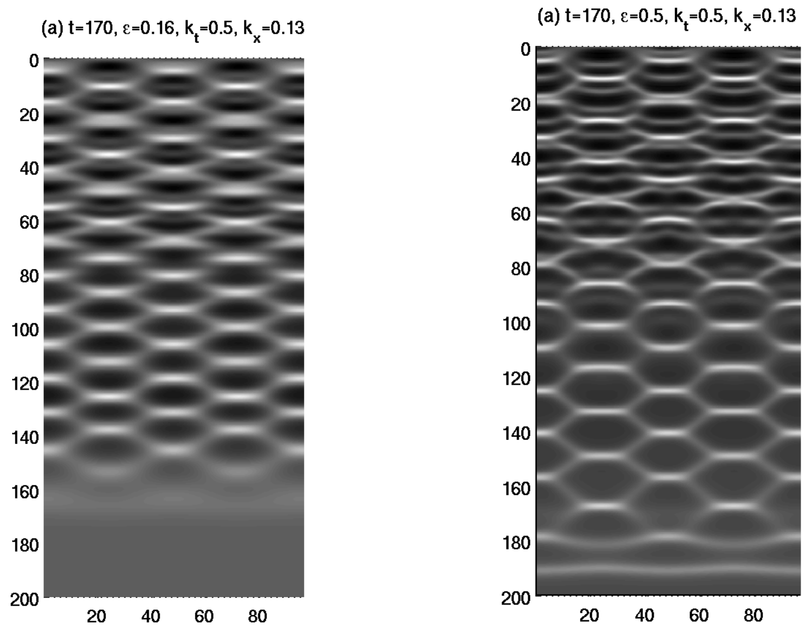

FIGURE 13. Surface profiles at $t = 170$ with (a) $\epsilon = 0.16$ and (b) $\epsilon = 0.5$.

The wave patterns for $\epsilon = 0.16$ and $\epsilon = 0.50$ at $t = 170$ are shown in Figure 13. Together with Figure 12(a), we can conclude that larger ϵ generates pattens with bigger y-wave length. To be more precise, we compute four main parameters of the resulting wave patterns and list them in Table 4 for each ϵ.

In Table 4, F_{max} denotes peak value of the pattern, which is computed by averaging three peak values, A_{max} denotes the amplitude of the pattern, $A = F_{max} - F_{min}$, where F_{min} is computed by averaging three trough values. L_y denotes the wave number in y-direction and L_t denotes the wave number in t-direction. For ϵ small, F_{max} should be close to ϵ, A to 2ϵ, L_t to k_t and L_y to k_y. It is observed that L_x, which is the wave number in x direction is the same as k_x for the computations we performed.

From Table 4, one sees that F_{max} and A increase as ϵ increases, but A is less than 2ϵ for $\epsilon = 0.16, 0.30$ and 0.50. More precisely $F_{max} > \epsilon$ and $F_{min} > -\epsilon$. L_y is a decreasing function of ϵ, which is equivalent

ϵ	F_{max}	A	L_y	L_t
0.05	0.057	0.102	0.51	0.499
0.16	0.20	0.31	0.49	0.499
0.30	0.41	0.54	0.45	0.495
0.50	0.65	0.78	0.38	0.497

TABLE 4. Specifications of wave patterns generated with various ϵ when $k_x = 0.13, k_t = 0.50$ which yield $k_y = 0.5063$.

to say that y-wavelength is an increasing function of ϵ. L_t is almost a constant, close to k_t, for all ϵ. The speed the pattern moves in y-direction is therefore increasing as ϵ increases, which can be observed by investigating Figure 12(a) and Figure 13.

To see more details of the wave profile, two slices of the wave in the case $\epsilon = 0.50$ are plotted. In Figure 14(a), $(\eta, u, v)(x, 118.3, 170)$ is plotted. We remark that at $x = 0$ and $x = L$, u is zero, η and v are flat, which show that the solution satisfies (BC2) at $y = 118.3$ and $t = 170$, which is a randomly chosen point. The wave profile $(\eta, u, v)(0, y, 170)$ against y is plotted in Figure 14(b). We observe now that u is zero for all y. It is also observed that in the region where the pattern is formed, $y \in (100, 150)$ (see also Figure 13(b)), the crest is narrower and the trough is more flat, which corresponds precisely what were observed in laboratory experiments.

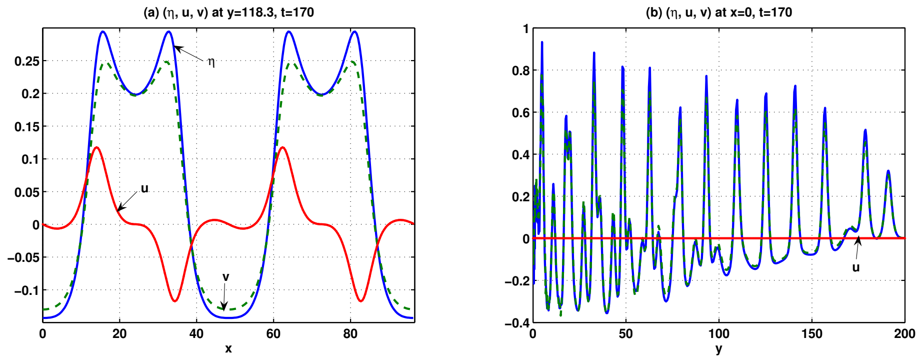

FIGURE 14. (a) Values of (η, u, v) at $y = 118.3$ and (b) at $x = 0$. Both plots are at $t = 170$ and with $\epsilon = 0.5$.

In order to shed some light on the stability of the code, additional calculations are performed with various time step sizes in the case of $\epsilon = 0.5$ with 256×1024 modes in the domain $[0, 48.3] \times [0, 200]$. The code works perfectly for Δt less or equal than 0.3, but blows up for $\Delta t = 0.4$.

5.3. **Wave patterns with various k_t and with various k_x.** Calculations for various k_t, with k_x and ϵ fixed are also performed. Two samples of wave profiles at $t = 170$ are shown in Figure 15, for $k_t = 0.40$ in (a) and for $k_t = 0.60$ in (b), and both with $\epsilon = 0.16$ and $k_x = 0.13$. Together with Figure 13(a) which is for $k_t = 0.50$ with the same k_x and ϵ, one observes that L_y increases as k_t increases. With a similar calculation as in Section 5.2, we also observe that F_{max} and A decreases as k_t increases. Furthermore, the transition period is longer with smaller k_t.

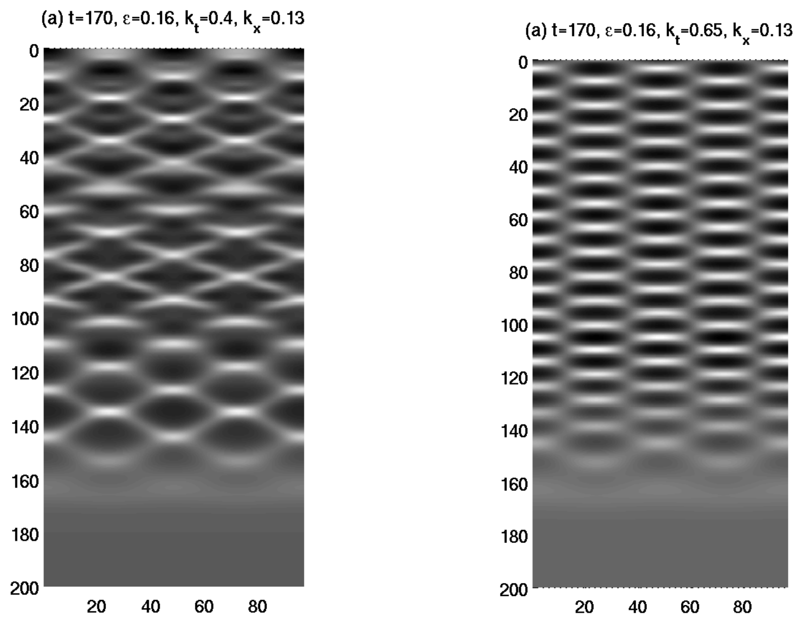

FIGURE 15. Wave profiles for $k_t = 0.40$ and $k_t = 0.65$, and both with $\epsilon = 0.16$ and $k_x = 0.13$.

Similar calculations are conducted for various k_x with k_t and ϵ fixed. Surface profiles for $k_x = 0.20$ and $k_x = 0.30$ are shown in Figure 16 with $k_t = 0.50$ and $\epsilon = 0.16$ and at $t = 170$. Three and four x-periods instead of two are shown, just for balancing the x and y coordinates. Together with Figure 13(a), we observe that L_y decreases as k_x increases and the change in A is small, if there is any. In all cases in Section 5, it appears that $L_x = k_x$, L_t is close to k_t.

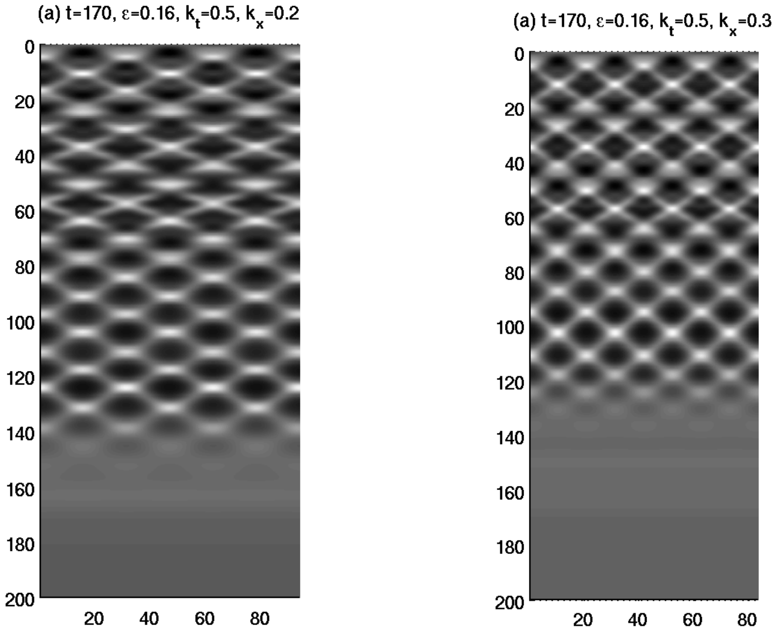

FIGURE 16. Wave profiles for $k_x = 0.20$ and $k_x = 0.30$, and both with $\epsilon = 0.16$ and $k_t = 0.50$.

The goal of this section is to shed some light on the wave patterns generated with only boundary data. Detailed analysis on the relationship between F_{max}, A, L_x, L_t and L_y (a "nonlinear" dispersion relation) and the comparison with laboratory experiments and with other water wave equations will be carried out elsewhere.

Acknowledgment. The author wishes to thank Professor J. Shen (Purdue University) for his help in writing the code.

References

[1] J. P. Albert, A. Alazman, J. L. Bona, M. Chen, and J. Wu, *Comparisons between the BBM equation and a Boussinesq system*, Advances in Differential Equations, 11 (2006), pp. 121–166.

[2] B. Alvarez-Samaniego and D. Lannes, *Large time existence for 3d water waves and asymptotics*, (preprint).

[3] J. L. Bona and M. Chen, *A Boussinesq system for two-way propagation of nonlinear dispersive waves*, Physica D, 116 (1998), pp. 191–224.

[4] J. L. Bona, M. Chen, and J.-C. Saut, *Boussinesq equations and other systems for small-amplitude long waves in nonlinear dispersive media I: Derivation and the linear theory*, J. Nonlinear Sci., 12 (2002), pp. 283–318.

[5] ——, *Boussinesq equations and other systems for small-amplitude long waves in nonlinear dispersive media II: Nonlinear theory*, Nonlinearity, 17 (2004), pp. 925–952.

[6] J. L. Bona, T. Colin, and D. Lannes, *Long wave approximations for water waves*, Arch. Ration. Mech. Anal., 178 (2005), pp. 373–410.

[7] ——, *Long wave approximations for water waves*, Arch. Ration. Mech. Anal., 178 (2005), pp. 373–410.

[8] J. V. Boussinesq, *Théorie générale des mouvements qui sont propagés dans un canal rectangulaire horizontal*, C. R. Acad. Sci. Paris, 73 (1871), pp. 256–260.

[9] C. Canuto, M. Y. Hussaini, A. Quarteroni, and T. A. Zang, *Spectral Methods in Fluid Dynamics*, Springer-Verlag, 1987.

[10] F. Chazel, *Influence of bottom topography on long water waves*, M2AN, 41 (2007), pp. 771–799.

[11] H. Chen, M. Chen, and N. V. Nguyen, *Cnoidal wave solutions to boussinesq systems*, submitted to Nonlinearity, (2006).

[12] M. Chen, *Exact traveling-wave solutions to bi-directional wave equations*, International Journal of Theoretical Physics, 37 (1998), pp. 1547–1567.

[13] ——, *Equations for bi-directional waves over an uneven bottom*, Mathematics and Computers in Simulation, 62 (2003), pp. 3–9.

[14] M. Chen and G. Iooss, *Periodic Wave Patterns of two-dimensional Boussinesq systems*, European Journal of Mechanics B/Fluids, 25 (2006), pp. 393–405.

[15] ——, *Asymmetrical Periodic Wave Patterns of two-dimensional Boussinesq systems*, (to appear in Physica D.).

[16] P. Daripa and R. K. Dash, *A class of model equations for bi-directional propagation of capillary-gravity waves*, Internat. J. Engrg. Sci., 41 (2003), pp. 201–218.

[17] D. Fuhrman and P. Madsen, *Short-crested waves in deep water: A numerical investigation of recent laboratory experiments*, JFM, (2005), p. to appear.

[18] S. Grilli, M. Ioualalen, J. Asavanant, F. Shi, J. Kirby, and P. Watts, *Source constraints and model simulation of the december 26, 2004 indian ocean tsunami*, J. Water. Port. Coast. Ocean Engnr, 133 (2007).

[19] J. L. Hammack, D. M. Henderson, and H. Segur, *Progressive waves with persistent two-dimensional surface patterns in deep water*, J. Fluid Mech., 532 (2005), pp. 1–51.

[20] D. Lannes, *Well-posedness of the water-waves equations*, J. Amer. Math. Soc., 18 (2005), pp. 605–654 (electronic).

[21] P. Madsen and H. A. Schäffer, *Higher-order Boussinesq-type equations for surface gravity waves: derivation and analysis*, Phil. Trans. R. Soc. Lond. A, 356 (1998), pp. 3123–3184.

[22] D. H. Peregrine, *Equations for water waves and the approximation behind them*, in Waves on beaches and resulting sediment transport; proceedings of an advanced seminar conducted by the Mathematics Research Center, Univ. Wisconsin, Academic Press: New York, 1972, pp. 95–121.

[23] J. Shen, *Efficient spectral-Galerkin method I. direct solvers for second- and fourth-order equations by using Legendre polynomials*, SIAM J. Sci. Comput., 15 (1994), pp. 1489–1505.

[24] ———, *Efficient spectral-Galerkin method II. direct solvers for second- and fourth-order equations by using Chebyshev polynomials*, SIAM J. Sci. Comput., 16 (1995), pp. 74–87.
[25] S. Wu, *Well-posedness in Sobolev spaces of the full water wave problem in 3-D*, J. Amer. Math. Soc., 12 (1999), pp. 445–495.